White Rose Research Online
eprints@whiterose.ac.uk
https://eprints.whiterose.ac.uk
Universities of Leeds, Sheffield and York

Deposited via The University of Leeds.

White Rose Research Online URL for this paper:
https://eprints.whiterose.ac.uk/id/eprint/164909/

Version: Accepted Version

Article:

Igoshev, AP, Hollerbach, R, Wood, T et al. (2021) Strong toroidal magnetic fields required by quiescent X-ray emission of magnetars. Nature Astronomy, 5 (2). pp. 145-149. ISSN: 2397-3366

https://doi.org/10.1038/s41550-020-01220-z

© 2020, The Author(s), under exclusive licence to Springer Nature Limited. This is an author produced version of an article published in Nature Astronomy. Uploaded in accordance with the publisher's self-archiving policy.

Reuse

Items deposited in White Rose Research Online are protected by copyright, with all rights reserved unless indicated otherwise. They may be downloaded and/or printed for private study, or other acts as permitted by national copyright laws. The publisher or other rights holders may allow further reproduction and re-use of the full text version. This is indicated by the licence information on the White Rose Research Online record for the item.

Takedown

If you consider content in White Rose Research Online to be in breach of UK law, please notify us by emailing eprints@whiterose.ac.uk including the URL of the record and the reason for the withdrawal request.

UNIVERSITY OF LEEDS
University of Sheffield
UNIVERSITY of York

Strong toroidal magnetic fields required by quiescent X-ray emission of magnetars

Andrei P. Igoshev[*], Rainer Hollerbach[*], Toby Wood[†]
and Konstantinos N. Gourgouliatos[‡]

August 26, 2020

Magnetars are neutron stars (NSs) with extreme magnetic fields[1] of strength $5 \times 10^{13} - 10^{15}$ G. These fields are generated by dynamo action during the proto-NS phase, and are expected to have both poloidal and toroidal components[2,3,4,5,6], although the energy of the toroidal component could be ten times larger[7]. Only the poloidal dipolar field can be measured directly, via NS spin-down[8]. The magnetic field provides heating and governs how this heat flows through the crust[9]. Magnetar thermal X-ray emission in quiescence is modulated with the rotational period of the NS, with a typical pulsed fraction 10-58%, implying that the surface temperature is significantly non-uniform despite the high thermal conductivity of the star's crust. Poloidal dipolar fields cannot explain this large pulsed fraction[10,11]. Previous 2D simulations[12,13] have shown that a strong, large-scale toroidal magnetic field pushes a hot region into one hemisphere and increases the pulsed fraction. Here, we report 3D magneto-thermal simulations of magnetars with strong large-scale toroidal magnetic fields. These models, combined with ray propagation in curved space-time, accurately describe the observed light-curves of 10 out of 19 magnetars in quiescence and allow us to further constrain their rotational orientation. We find that the presence of a strong toroidal magnetic field is enough to explain the strong modulation of thermal X-ray emission in quiescence.

Here we investigate the formation and evolution of hotter and colder regions at the surface of a quiescent magnetar, using three-dimensional magnetohydrodynamic (MHD) simulations in a spherical shell performed with a modified version of the `PARODY` code[14] (see Methods Section 1). We simulate the magneto-thermal evolution for two field configurations that have strong toroidal fields containing 90% of the total magnetic energy: in model A the poloidal and toroidal components are aligned, and in model B the toroidal magnetic field is inclined by 45° with respect to the poloidal dipole. The initial surface, poloidal, dipole magnetic field at the pole is 4.4×10^{13} G (model A) and 4×10^{13} G (model B); the maximum values of magnetic field in the crust at the beginning of the simulations are 1.2×10^{15} G. Figure 1 shows the surface tem-

---

[*] Department of Applied Mathematics, University of Leeds, Leeds LS2 9JT, UK

[†] School of Mathematics, Statistics and Physics, Newcastle University, Newcastle upon Tyne, NE1 7RU, UK

[‡] Department of Physics, University of Patras, 26504, Patras, Greece

perature distribution for these models after about 20 Kyr of evolution. The isothermal, purely magnetic properties of these models have previously been studied in detail[15], but without the heat diffusion equation included here. The filamentary pattern of hot and cold regions visible in Figure 1 reflects the magnetic field structure arising from an instability of the toroidal field[16]. Both models exhibit north-south asymmetry: model A has a hot zone that wraps around the dipole axis, whereas model B has a single hot spot. The results for model A are consistent with earlier results obtained using a 2D axisymmetric model[12,13]. Models analogous to our model B with thermal emission have never previously been computed.

We also compute three auxiliary models C, D and E, see surface temperature maps in Extended Data Figures 1 and 2. In models C and D the initial magnetic fields have pure poloidal, dipole configuration with strengths of 7×10^{13} G and 5×10^{14} G respectively. In model E the poloidal and toroidal components of magnetic field have similar energy. The initial dipolar poloidal magnetic field at the north magnetic pole is 10^{14} G.

We further compute the light-curves produced by each of these models (see Methods Section 2 for details) taking into account relativistic effects. We assume that the NS has radius $R = 10$ km and mass $M = 1.4\ M_{\odot}$. Because magnetars rotate relatively slowly, we use approximations for ray propagation in the Schwarzschild metric. We use a simplified beaming function which follows the trend of detailed atmosphere calculations[17], but does not depend on magnetic field and temperature. For a given surface temperature map, the light-curve depends on three angular parameters: κ, the angle between the magnetic poloidal moment and the rotation axis, i, the angle between the observer's line of sight and the rotation axis, and $\Delta\Phi$, the phase shift.

We find that models A and B have bolometric thermal X-ray luminosities of $0.8 - 2 \times 10^{32}$ erg/s (no neutrino cooling is assumed and the core temperature is fixed at 10^8 K, so these are indicative of typical 10 Kyr age) and pulsed fraction ranges from 16 to 53 per cent for soft X-ray, which is consistent with observations of magnetars in quiescence. By contrast, models that have weak toroidal magnetic fields have a temperature distribution that is very symmetric with respect to the magnetic equator[13] (see Extended data Figures 1, 2 and 3), and typically have a maximum pulsed fraction of $\lessapprox 10\% - 20\%$. A hot region wrapped around the dipole poloidal axis (as in model A) produces a light-curve symmetric around rotational phase 0.5. A small single hot spot (as in model B) produces light-curves which are asymmetric around phase 0.5.

First, we fit our light-curves to the folded soft X-ray emission of all transient magnetars in quiescence with $L_X \lesssim 10^{33}$ erg/s for energy range 0.3-10 KeV. Second, we fit our model to persistent magnetars. The reason we initially select transient magnetars is that for persistent magnetars alternative heating mechanisms could play an essential role, such as ambipolar diffusion or magnetospheric heating of the surface. The details of the observational reduction and the fitting procedure can be found in Methods Sections 3 and 4 respectively. In brief, we reanalyse existing observations (see Extended data Figure 4) of magnetars in quiescence and produce period-folded light-curves in the soft X-ray range 0.3-2 KeV.

The parameters that produce the best fit in each case are summarised in Table 1. For the four transient magnetars SGR 0418+5729, 1E 1547.0-5408, XTE J1810-197 and Swift J1822.3-1606 and high-magnetic field pulsar J1119-6127 we obtain perfectly acceptable fits; see examples in Figure 2 (remaining light-curves can be found in Extended Data Figures 5-8). In the case of CXOU J164710.0-455216 our fit is marginally acceptable, producing a compact hot region which was impossible in 2D simulations[12]. The temperature distribution produced as a result of magneto-thermal evolution in the crust describes extremely well the soft X-ray emission of these objects in quiescence. The asymmetries previously found in the light-curve are naturally explained by a single hot spot formed by an intense, large-scale toroidal field misaligned with the dipole axis. We also compute a measure of asymmetry for the profile (See Method 6). On average the model A better describes light-curves with smaller asymmetry and B better describes light-curves with larger asymmetry. We briefly discuss three cases that are described less successfully by our model in Methods Section 5 and show light-curves in Extended Data Figures 9 and 10. One caveat for our analysis is that some of the magnetars in our list have magnetic dipole strengths of 10^{14} G, compared to 4×10^{13} G for models A and B.

Our estimate for the angle $\kappa = 109^\circ$ for 1E 1547.0-5408 is somewhat different from the value inferred from radio observations[18] $\kappa = 160^\circ$. Fitting against model B at the age 24 Kyr gives a very different angle, $\kappa \approx 16^\circ$ ($\chi^2 = 14$), which is a nearly aligned rotator and agrees better with the radio data. This means that for some sources there could exist some degeneracy between the parameters describing the star's rotational orientation and the misalignment between poloidal and toroidal magnetic field. Additional simulations and observations will be required to test this.

Fitting light-curves of persistent magnetars, we find that our model reproduces four objects: 4U 0142+61, CXOU J171405.7-381031, 1E 1841-045 and SGR 1900+14. Although the fits are formally acceptable, we cannot compare the luminosities in this case, because our simulations lack important physics such as neutrino cooling.

When we fit the small pulsed fraction, symmetric light-curves of SGR 1900+14, 4U 0142+61 and SGR 0501+4516 using models D and E we get comparable χ^2. So, SGR 1900+14 can be described using model D ($\chi^2 = 21.4$) or E ($\chi^2 = 21.1$). 4U 0142+61 can be described using model E ($\chi^2 = 20.8$). SGR 0501+4516 is slightly better (still missing important features) described by model E ($\chi^2 = 82.2$).

Our models only describe the magnetic field evolution in the NS crust. Further work is needed to better understand the magnetic field evolution in the NS core, where ambipolar diffusion might play an important role[19,20], particularly in very young NSs. Soft thermal emission of some magnetars could be caused by the magnetospheric currents which could increase surface temperature. Our results crucially depend on two main assumptions: (1) the magnetic field is crust confined and the toroidal component is dipolar and (2) strong beaming for thermal radiation which agrees with detailed numerical simulations[17]. The process responsible for formation of this toroidal magnetic field is unknown at the moment. A toroidal field with this structure is needed to stabilise the poloidal dipolar field in MHD equilibrium[7], but this field penetrates the core, which is not the case in our simulations.

The large-scale toroidal magnetic field, which is the main source of the magnetospheric twist, could also cause crust yielding if strong enough. We have shown that the same toroidal magnetic field can naturally explain the X-ray emission of quiescent magnetars. Therefore, possibly the main difference between a magnetar and a strongly magnetised NS which shows no magnetar-like behaviour is the strength of the toroidal magnetic field in the crust. With the revolutionary insight obtained by the NICER telescope for recycled pulsars[21,22], it is becoming increasingly clear that the magnetic field structure of NSs is complicated, so it is extremely important to explore the process of magnetic field evolution and formation for NSs. An alternative candidate for a "hidden" component is a small-scale poloidal magnetic field. The effects produced by such a field need to be studied both in magnetospheric and crust simulations.

References

[1] Kaspi, V. M. & Beloborodov, A. M. Magnetars. *Ann. Rev. Astron. Astroph.* **55**, 261–301 (2017).

[2] Ferrario, L., Melatos, A. & Zrake, J. Magnetic field generation in stars. *SSRv* **191**, 77–109 (2015).

[3] Braithwaite, J. & Spruit, H. C. A fossil origin for the magnetic field in A stars and white dwarfs. *Nature* **431**, 819–821 (2004).

[4] Thompson, C., Lyutikov, M. & Kulkarni, S. R. Electrodynamics of magnetars: Implications for the persistent X-ray emission and spin-down of the soft gamma repeaters and anomalous X-ray pulsars. *Astrophys. J.* **574**, 332–355 (2002).

[5] Lyutikov, M. & Gavriil, F. P. Resonant cyclotron scattering and Comptonization in neutron star magnetospheres. *Mon. Not. R. Astron. Soc.* **368**, 690–706 (2006).

[6] Rea, N., Zane, S., Turolla, R., Lyutikov, M. & Götz, D. Resonant cyclotron scattering in magnetars' emission. *Astrophys. J.* **686**, 1245–1260 (2008).

[7] Braithwaite, J. & Nordlund, Å. Stable magnetic fields in stellar interiors. *Astron. Astrophys.* **450**, 1077–1095 (2006).

[8] Gunn, J. E. & Ostriker, J. P. Magnetic dipole radiation from pulsars. *Nature* **221**, 454–456 (1969).

[9] Pons, J. A. & Viganò, D. Magnetic, thermal and rotational evolution of isolated neutron stars. *Living Reviews in Computational Astrophysics* **5**, 3 (2019).

[10] Özel, F., Psaltis, D. & Kaspi, V. M. Constraints on thermal emission models of anomalous X-ray pulsars. *Astrophys. J.* **563**, 255–266 (2001).

[11] Hu, C.-P., Ng, C. Y. & Ho, W. C. G. A systematic study of soft X-ray pulse profiles of magnetars in quiescence. *Mon. Not. R. Astron. Soc.* **485**, 4274–4286 (2019).

[12] Perna, R., Viganò, D., Pons, J. A. & Rea, N. The imprint of the crustal magnetic field on the thermal spectra and pulse profiles of isolated neutron stars. *Mon. Not. R. Astron. Soc.* **434**, 2362–2372 (2013).

[13] Viganò, D. *et al.* Unifying the observational diversity of isolated neutron stars via magneto-thermal evolution models. *Mon. Not. R. Astron. Soc.* **434**, 123–141 (2013).

[14] Wood, T. S. & Hollerbach, R. Three-dimensional simulation of the magnetic stress in a neutron star crust. *Phys. Rev. Lett.* **114**, 191101 (2015).

[15] Gourgouliatos, K. N. & Hollerbach, R. Magnetic axis drift and magnetic spot formation in neutron stars with toroidal fields. *Astrophys. J.* **852**, 21 (2018).

[16] Gourgouliatos, K. N. & Pons, J. A. Nonaxisymmetric Hall instability: A key to understanding magnetars. *Physical Review Research* **1**, 032049 (2019).

[17] van Adelsberg, M. & Lai, D. Atmosphere models of magnetized neutron stars: QED effects, radiation spectra and polarization signals. *Mon. Not. R. Astron. Soc.* **373**, 1495–1522 (2006).

[18] Camilo, F., Reynolds, J., Johnston, S., Halpern, J. P. & Ransom, S. M. The Magnetar 1E 1547.0-5408: Radio spectrum, polarimetry, and timing. *Astrophys. J.* **679**, 681–686 (2008).

[19] Passamonti, A., Akgün, T., Pons, J. A. & Miralles, J. A. On the magnetic field evolution time-scale in superconducting neutron star cores. *Mon. Not. R. Astron. Soc.* **469**, 4979–4984 (2017).

[20] Gusakov, M. E., Kantor, E. M. & Ofengeim, D. D. Evolution of the magnetic field in neutron stars. *Phys. Rev. D.* **96**, 103012 (2017).

[21] Riley, T. E. *et al.* A NICER View of PSR J0030+0451: Millisecond pulsar parameter estimation. *Astrophys. J. Lett.* **887**, L21 (2019).

[22] Bilous, A. V. *et al.* A NICER View of PSR J0030+0451: Evidence for a global-scale multipolar magnetic field. *Astrophys. J. Lett.* **887**, L23 (2019).

Correspondence

Correspondence should be addressed to Andrei Igoshev and Rainer Hollerbach.

Acknowledgements

We thanks Daniele Viganò and Frank Verbunt for valuable comments which helped to improve our work significantly. This work was supported by STFC grant No. ST/S000275/1. The numerical simulations were carried out on the STFC-funded DiRAC I UKMHD Science Consortia machine, hosted as part of and enabled through the ARC3 HPC resources and support team at the University of Leeds.

Authors contributions

All authors contributed to the simulation design, interpretation and writing the manuscript. A.P.I. carried out the X-ray data reduction, the MHD simulations and the model fitting. T.S.W. adapted the PARODY code to solve magneto-thermal equations.

Competing financial interests

The authors declare no competing financial interests.

Source name	Type p/t	κ (°)	i (°)	$\Delta\Phi$ (°)	Age (Kyr)	Model	χ^2/d.o.f.	As
4U 0142+61	p	33 ± 1	71 ± 1	178 ± 2	8.2	A	22/13	0.07
SGR 0418+5729	t	232 ± 24	271 ± 21	217 ± 9	24.0	B	8.2/13	0.58
PSR J1119-6127	t	186 ± 61	58 ± 31	76 ± 25	2.3	B	7.2/13	0.3
1E 1547.0-5408	t	109 ± 12	29 ± 3	175 ± 5	17.7	A	9.3/13	0.13
CXOU J164710.0-455216	t	215 ± 30	77 ± 22	34 ± 6	31.7	B	25.4/13	0.56
CXOU J171405.7-381031	p	177 ± 8	88 ± 10	11 ± 7	13	B	24.7/13	0.25
XTE J1810–197	t	149 ± 4	34 ± 6	160 ± 5	18	A	14.5/13	0.22
Swift J1822.3-1606	t	201 ± 40	284 ± 17	217 ± 6	13.6	B	19.4/13	0.38
1E 1841-045	p	44 ± 15	162 ± 5	160 ± 15	4	B	10/13	0.40
SGR 1900 + 14	p	114 ± 11	29 ± 9	188 ± 12	1.5	A	21/13	0.31
SGR 0501+4516	t	103	76	176	6.5	A	87.5/13	0.4
1RXS J170849.0-400910	p	238	115	20	13	B	52/13	1.1
3XMM J185246.6+003317	t	220	79	36.7	37	B	42.8/13	0.12

Table 1: **Best-fit parameters for the folded X-ray light-curves of magnetars.** Error bars are 95% confidence intervals. Ages presented in the table are ages of the best fit models. These ages might differ from actual age of the star because no cooling is assumed. We divide the table into two parts: where the fit could be accepted based on the χ^2/d.o.f. and where the fit clearly lacks important features of the observations. Type t stands for transient and p for persistent magnetar. As shows the mean value of absolute differences between left and right parts of the observed light-curve divided by the pulsed fraction. This value is a measure for how asymmetric observed light-curve is.

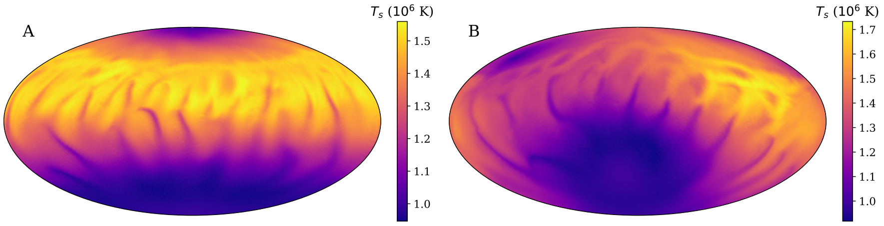

Fig. 1: **Surface temperature, T_s, maps obtained in 3D magneto-thermal simulations.** A: model A for NS with aligned poloidal and toroidal magnetic fields, age 18 Kyr. B: model B for NS with poloidal and toroidal magnetic fields inclined by angle of 45°, age 24 Kyr. The surface temperatures are in units of MK.

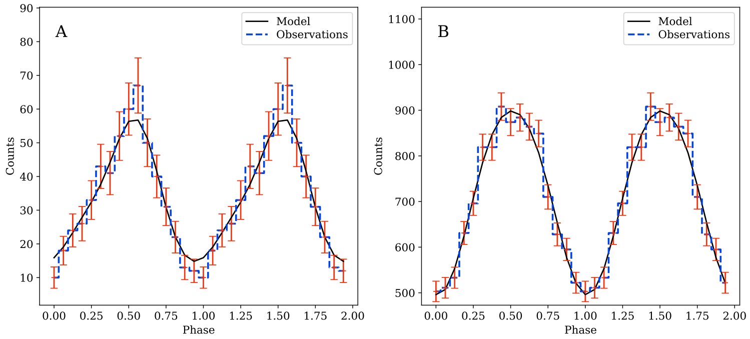

Fig. 2: **Folded soft X-ray light-curve (300-2000 eV) for magnetars.** A: SGR 0418+5729, B: 1E 1547.0-5408. The dashed blue lines and red error bars are observations and 1σ confidence intervals. The solid black lines are the theoretical light-curve for the most favourable orientation.

Methods

1 MHD and thermal simulations

We integrate the two coupled equations describing magnetic induction and heat transfer within the NS crust:

$$\frac{\partial \vec{B}}{\partial t} = -c\nabla\times\left\{\frac{1}{4\pi e n_e}(\nabla\times\vec{B})\times\vec{B} + \frac{c}{4\pi\sigma}\nabla\times\vec{B} - \frac{1}{e}S_e\nabla T\right\}, \tag{1}$$

$$C_V\frac{\partial T}{\partial t} = \nabla\cdot(\hat{k}\cdot\nabla T) + \frac{|\nabla\times\vec{B}|^2c^2}{16\pi^2\sigma} + \left(\frac{c}{4\pi e}\right)T\nabla S_e\cdot(\nabla\times\vec{B}). \tag{2}$$

Here $\vec{B}$ is the magnetic field, T is the temperature, c is the speed of light, e is the elementary charge, n_e is the electron density, S_e is the electron entropy, σ is the electrical conductivity, C_V is the crust heat capacity, and $\hat{k}$ is the thermal conductivity tensor. We use the equation of state for a degenerate, relativistic Fermi gas, and the Wiedemann–Franz law:

$$S_e = \left(\frac{\pi^4}{3n_e}\right)^{1/3}\frac{k_B^2T}{c\hbar}, \quad \text{and} \quad (\hat{k}^{-1})_{ij} = \frac{3e^2}{\pi^2k_B^2T}\left(\frac{1}{\sigma}\delta_{ij} + \frac{\varepsilon_{ijk}B_k}{ecn_e}\right), \tag{3}$$

where k_B is Boltzmann's constant, and $\hbar$ is Planck's constant.

The induction equation (1) describes the evolution of the magnetic field due to the Hall effect, Ohmic decay, and the Biermann battery. Our previous work[14,15 23] included only this equation, and without the Biermann battery term. The heat equation (2) describes the evolution of temperature due to anisotropic heat diffusion, Ohmic heating, and electron entropy advection. In both equations the final term is generally small, but is included for completeness. On the timescales of interest the heat capacity of the crust is negligible, but for numerical convenience we include a small heat capacity C_V that is proportional to σT. We use the same density and conductivity profiles as previous work[23]. The initial magnetic field configuration is described as:

$$\vec{B} = \nabla \times \nabla \times (V_{pu}\vec{r}) + \nabla \times (V_{tu}\vec{r}) \tag{4}$$

where V_{pu} and V_{tu} are the scalar fields describing the poloidal and toroidal components respectively. These fields are defined using spherical polar coordinates as

$$\begin{aligned} V_{pu} = B_0 \frac{\sqrt{3}\sqrt{1-e_t}}{r} \cos\theta(&734.5987631 - 2333.649604r \\ &+ 2465.151852r^2 - 865.6887777r^3) \end{aligned} \tag{5}$$

and

$$V_{tu} = B_0 \sqrt{3e_t}\, 2739.401879 \cos(\theta + \theta_0)(1 - r)(r - 0.9) \tag{6}$$

where the parameter e_t determines the contribution of the toroidal component, and where θ_0 is the angle between the orientation of the poloidal and toroidal magnetic fields.

Equations (1) and (2) are solved within a spherical shell with 9 km $< r <$ 10 km using the pseudo-spectral code `PARODY`[24,25]. We use 128 numerical cells in the radial direction and spherical harmonics up to degree $l = 120$. The timestepping method is Crank–Nicolson for the Ohmic decay term, backward-Euler for the isotropic part of the heat diffusion, and Adams–Bashforth for the remaining terms. We use vacuum boundary conditions for the magnetic field at the upper boundary, and perfectly conducting boundary conditions at the lower boundary, assuming for simplicity that all magnetic flux is expelled from the core. The upper boundary condition for the temperature is the standard thermal-blanket relation[26]

$$-\vec{r} \cdot \hat{k} \cdot \nabla T|_b = \sigma_S T_s^4 \tag{7}$$

where σ_S is the Stefan–Boltzmann constant. We employ a simple relation between the surface temperature T_s, and the temperature at the top of the crust T_b:

$$\left(\frac{T_b}{10^8\ \mathrm{K}}\right) = \left(\frac{T_s}{10^6\ \mathrm{K}}\right)^2 . \tag{8}$$

The core is assumed to have a fixed temperature of 10^8 K.

The model physics is simplified in two respects: (1) We neglect any cooling by neutrinos, both in the core and in the crust. Neutrino cooling is important for the long-term temperature evolution, and for bursting behaviour, but is less relevant to temperature maps of the surface for the quiescent state of magnetars. (2) The electrical conductivity is assumed to be independent of temperature. These limitations will be addressed in future work.

2 Ray propagation and orientation of NS

To compute the corresponding light-curve from a thermal map taking into account effects of the general relativity we use a numerical method[27] with angles i and κ, where i is the angle between rotational axis and line of sight, and κ is the angle between the original magnetic dipole and rotational axis. Coordinates at the NS surface are computed with respect to the magnetic pole as θ, ϕ. This is different from previous work[27] where the hot spots are assumed to coincide with magnetic poles. This is not the case in our simulations, where hot regions are extended and located at a significant separation from magnetic poles. In a few cases we tried to optimise the NS radius and mass as well, but due to the low photon counts and slow rotation of magnetars the light-curve only depends weakly on the exact values of NS compactness. We therefore kept these parameters fixed during the optimisation process.

We convert the temperature obtained using the upper boundary condition to intensity of X-ray emission from a particular element at the NS surface using a simple blackbody model. We use a beaming factor proportional to $\cos^2 \alpha$, where α is the angle between the direction where a photon is emitted and normal to the surface at the emission point. This curve roughly follows the numerical beaming function[17] taking into account vacuum polarisation effects. This is nevertheless a simplification because the specific intensity emitted in a particular direction depends also on temperature, magnetic field strength, spectral band and orientation of the magnetic field at the surface. The function $\cos^2 \alpha$ correctly represents the trend but more detailed atmosphere calculations are required in the future.

To produce the light-curve, we integrate the flux which reaches the observer over the whole visible hemisphere for each rotational phase. We normalise the light-curve by mean luminosity of the source seen for this particular orientation. We notice that if the light-curve is symmetric around the phase 0.5 (i.e. the hot spot forms a belt), there is a degeneracy between angles i and κ. These two angles can be exchanged and in this case they produce a very similar light-curve. The light-curve would be exactly the same if the hot belt was a perfect band with no longitudinal variations in brightness. This degeneracy completely disappears if the hot spot is not extended, as in model B.

3 X-ray data reduction

We provide the observational IDs of dataset for magnetars in quiescence in Extended Data Figure 4; these are old observations[11]. To analyse the *Chandra* observations we use the software package CIAO[28] 4.12 together with the calibration database CALDB 4.9.0. The observations are reprocessed with help of `chandra_repro` package. During the analysis the McGill magnetar catalogue (http://www.physics.mcgill.ca/~pulsar/magnetar/main.html) was used extensively[29]. Only events from a region centred at the source (according to the catalogue) with radius of 4″ were extracted. Because we are interested in thermal quiescence emission, we filter out all photons outside of the 300-2000 eV energy interval. All times of arrival for events are transformed to the solar system baricentre using `axbary` tool together with the `DE-405` solar system ephemeris and orbital information provided by the *Chandra* data archive. We also visually inspected source and background light-curve to verify an absence of flares.

We search for the magnetar period using the fast Fourier transform (time resolution 0.5-3.5 sec depending on instrument mode) and period-folding (`pfold` package; 10 phase bins) for each individual observation and compared with ephemeris computed based on measurements of period and period derivative collected by different authors. If the rotational period is not seen in a particular observation, we disregard this dataset. If an observational period is hard to determine to four significant digits from individual observation, we use the ephemeris value. After this a folded light-curve with 16 phase-bins is produced.

The first folded light-curve is phase-shifted to place minimum photon count at phase 0. If the magnetar was observed multiple times, the following folded light-curves are produced following exactly the same procedure, but at the last step the phase-shift between different observations is determined using correlation function. The resulting light-curve is produced by summation of total number of photons in bins seen in different observations taking into account the phase-shift.

Working with the `XMM-Newton` observations we use `heasoft` 6.26.1 and `SAS` 18.0.0 packages. We filter time intervals with high background emission using filter `RATE<0.4` for energy range 10-12 KeV. We further extract events with energies in the range 300-2000 eV centred at the source position with extraction radius of 20 arcsec. Only single and double photon events `PATTERN<=4` for `PN` and `PATTERN<=12` for `MOS1` and `MOS2` are selected at this stage. All arrival times are transformed to the baricentre of the solar system using `barycen` task. We prefer to analyse the `PN` observations, but if a small number of photons is registered, we also added results from both `MOS1` and `MOS2` cameras. In the case of 3XMM J1852, we had to rely only on `MOS1` and `MOS2` observations similar to previous work[11]. When the light-curve is extracted, we follow the same procedure as in the case of the *Chandra* data and sum counts in individual phase bins, taking into account possible phase shift between observations.

4 Statistical analysis

After we obtain an observational folded X-ray light-curve, we perform optimisation of the model with fixed age searching for the most probable values of three continuous parameters κ, i and $\Delta\Phi$. To do so, we use the maximum likelihood technique with likelihood in form of C-statistics[30]. The optimum value is found using the Nelder-Mead algorithm[31]. When the most probable values are found, we perform optimisation for thermal maps occurring at other ages of the NS evolution. We choose the model and age which correspond to the lowest value of the C-statistics. We perform the optimisation this way, because each time-step of MHD simulations takes a lot of memory space, therefore we need to restrict a number of ages we perform optimisation for. We additionally check the quality of the final fit using the χ^2 test. The confidence intervals are computed for each parameter κ, i and $\Delta\Phi$ by fixing the other two parameters and searching for a new value of χ^2 statistics which differs from original value by 3.84 (95% probability for χ^2 with a single variable).

5 Cases not described by our model

In two cases, SGR 0501 and 3XMM J185246.6+003317, our model does not describe at least some essential features of the folded light-curve. Namely, in the case of SGR 0501 the central valley between two peaks is not deep enough, see Extended Data Figure 9 (left panel). Overall the folded light-curve is skewed while the model is symmetric. It is important to notice that the quiescence X-ray spectrum of SGR 0501 consists of two components: a blackbody and a power-law. The latter component is essential to describe the emission and indicates that the photons are strongly reprocessed in the magnetosphere. The inverse Compton scattering could change the light-curve significantly if the magnetosphere twist is large. Therefore, we predict that the light-curve of SGR 0501 could relax to a much simpler shape after a large outburst when the twist is released[5].

In the case of 3XMM J185246.6+003317, it is unclear how to form simultaneously a narrow profile typical for model B and two separate peaks typical for model A. In this case the counts are only extracted from MOS images and the number of counts is quite low, but is still enough to produce a reliable light-curve.

We analyse observations of strongly asymmetric source 1RXS J170849.0-400910. We found the best rotational orientation of the model B with age $\approx$ 13 Kyr to be $\kappa = 238$, $i = 115$ and $\Delta\Phi = 20$ with $\chi^2 = 52$. Although the χ^2 value is large and disregards our model, we believe that in this case the main reason for this is the beaming model and possibly neutrino cooling. As seen in Extended Data Figure 10, our profile follows the shape of the light-curve nearly perfectly, with differences at the level of few percent. Large χ^2 occurs because this is a bright source with a large number of photons per bin (4000 on average) so small details in the light-curve are visible.

We tried to analyse the source SGR J1745-2900. In two *Chandra* observations Obs ID 18731 and 18732 only 124 soft X-ray photons (0.3-2 KeV) were detected. We could not reliably identify the spin-period using either periodogram or period-folding. When we fold the soft X-ray counts using the period computed on the base of ephemeris, the resulting light-curve did not look similar to previous analysis[11], and does not seem significant. We experience a similar problem with SGR J1935+2154 (XMM PN Obs ID 0764820201). We managed to identify the correct period only when we take into account photons in energy range 0.3-10 KeV. We do not analyse these light-curves due to the lack of soft X-ray photons.

We did not try to fit complicated light-curves of some bright persistent magnetars such as CXOU J010043.1-721134 or 1E 2259+586 because these sources have light-curve morphology which we have never seen in our simulations. 1E 1048.1-5937 has large pulsed fraction and light-curve morphology which we cannot reproduce with our models.

6 Measure of the light-curve asymmetry

We compute the asymmetry of a soft X-ray light curve using following equation:

$$As = \frac{F_{\max} + F_{\min}}{F_{\max} - F_{\min}} \sum_{i=1}^{N} |F_{i-c} - F_{i+c}| \tag{9}$$

where F_c is the flux at central phase. We determine the central phase as the rotational phase where the maximum is located (if profile has a single maximum) or as a point of symmetry which minimised the As value. The factor in front of sum is the inverse pulsed fraction. If the light-curve is absolutely symmetric, we expect $As = 0$.

Data Availability Statement

The data that support the plots within the paper and other findings are provided in electronic form together with the paper.

Code Availability Statement

The codes that were used to prepare our models within the paper are available from the corresponding authors upon reasonable request.

References

[23] Gourgouliatos, K. N., Wood, T. S. & Hollerbach, R. Magnetic field evolution in magnetar crusts through three-dimensional simulations. *Proceedings of the National Academy of Science* **113**, 3944–3949 (2016).

[24] Dormy, E., Cardin, P. & Jault, D. MHD flow in a slightly differentially rotating spherical shell, with conducting inner core, in a dipolar magnetic field. *Earth and Planetary Science Letters* **160**, 15–30 (1998).

[25] Aubert, J., Aurnou, J. & Wicht, J. The magnetic structure of convection-driven numerical dynamos. *Geophysical Journal International* **172**, 945–956 (2008).

[26] Gudmundsson, E. H., Pethick, C. J. & Epstein, R. I. Structure of neutron star envelopes. *Astrophys. J.* **272**, 286–300 (1983).

[27] Beloborodov, A. M. Gravitational bending of light near compact objects. *Astrophys. J. Lett.* **566**, L85–L88 (2002).

[28] Fruscione, A. *et al.* CIAO: Chandra's data analysis system. In *Proceedings of the SPIE*, vol. 6270 of *Society of Photo-Optical Instrumentation Engineers (SPIE) Conference Series*, 62701V (2006).

[29] Olausen, S. A. & Kaspi, V. M. The McGill Magnetar Catalog. *Astrophys. J. Supp. Ser.* **212**, 6 (2014).

[30] Cash, W. Parameter estimation in astronomy through application of the likelihood ratio. *Astrophys. J.* **228**, 939–947 (1979).

[31] Nelder, J. A. & Mead, R. A simplex method for function minimization. *The Computer Journal* **7**, 308–313 (1965).

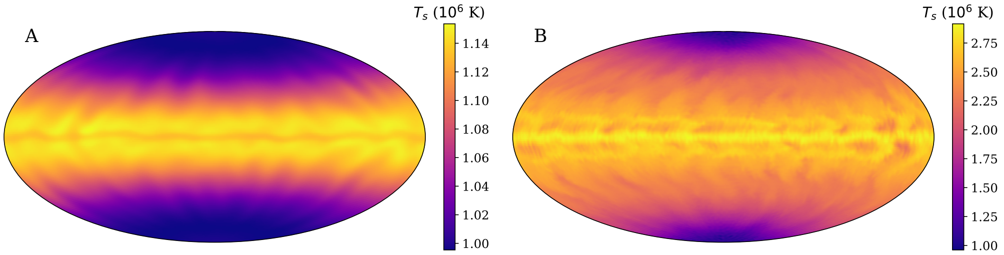

Figure 1: **Surface temperature, T_s, maps obtained for models with no initial toroidal magnetic field.** A: model C for NS with initial dipolar poloidal magnetic field $B_0 = 7 \times 10^{13}$ G at age 10 Kyr. B: model D for NS with initial poloidal dipolar magnetic field $B_0 = 5 \times 10^{14}$ G age 10 Kyr. The surface temperatures are in units of MK.

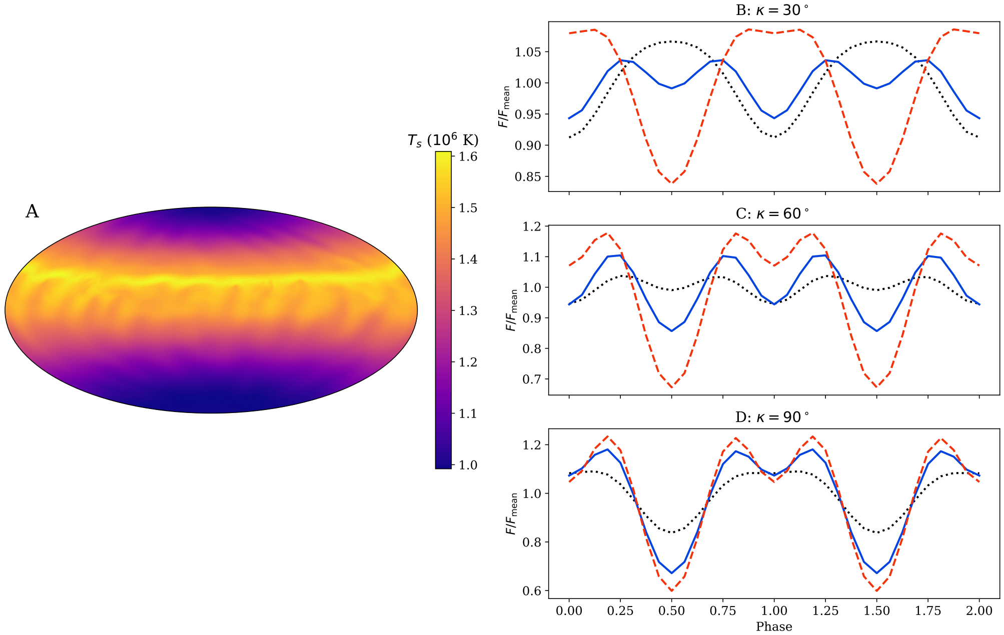

Figure 2: **Results for model E with equal initial energy in toroidal and poloidal magnetic fields** Panel A: surface temperature, T_s, maps obtained in 3D magneto-thermal simulations. We show NS with initial dipolar poloidal magnetic field $B_0 = 1 \times 10^{14}$ G at age 10 Kyr. Panels B, C, D: the soft X-ray light-curves expected for this thermal map at 10 Kyr. Panel B shows $\kappa = 30^\circ$, panel C shows $\kappa = 60^\circ$ and panel D shows $\kappa = 90^\circ$. Dotted black lines correspond to $i = 30^\circ$, solid blue lines correspond to $i = 60^\circ$ and red dashed lines correspond to $i = 90^\circ$.

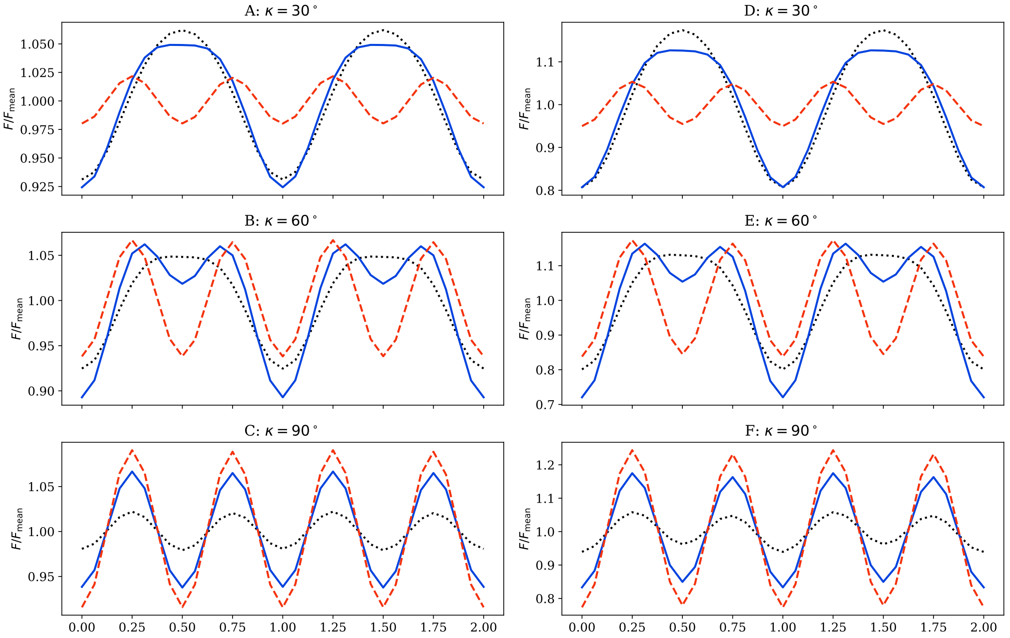

Figure 3: **The soft X-ray light-curves expected for models with no initial toroidal magnetic field.** Panels A,B,C are for model C, panels D,E,F are for model D. Panels A and D show $\kappa = 30^\circ$, panels B and E show $\kappa = 60^\circ$ and panels C and F show $\kappa = 90^\circ$. Dotted black lines correspond to $i = 30^\circ$, solid blue lines correspond to $i = 60^\circ$ and red dashed lines correspond to $i = 90^\circ$.

Source name	Instrument/mode	Obs ID
4U 0142+61	*Chandra*/CC	724, 6723, 7659
SGR 0418+5729	*Chandra*/TE	13148, 13235, 13236
SGR 0501+4516	*Chandra*/TE	14811, 15564
PSR J1119-6127	*XMM Newton*/PN	0150790101
1E 1547.0–5408	*XMM Newton*/PN	0604880101
CXOU J164710.0–455216	*XMM Newton*/PN and MOS	0404340101
1RXS J170849.0 - 400910	*Chandra*/CC	4605
CXOU J171405.7-381031	*Chandra*/CC	10113, 11233, 13749, 16762, 16763
XTE J1810–197	*Chandra*/TE	13746, 13747, 15870, 15871
Swift J1822.3–1606	*Chandra*/TE	14819, 15988, 15989, 15992, 15993
1E 1841-045	*Chandra*/CC	730
3XMM J185246.6+003317	*XMM Newton*/MOS	0550671301, 0550671801, 0550671901
SGR1900+14	*Chandra*/CC	3863, 3864, 8215

Figure 4: **Data sets analysed**

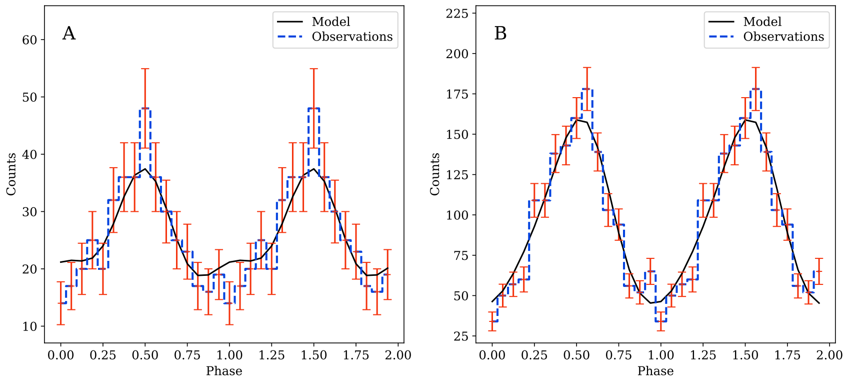

Figure 5: **Folded soft X-ray light-curve (300-2000 eV) for magnetars.** A panel: PSR J1119-6127, B panel CXOU J164710.0-455216. Dashed blue lines show observations, and the theoretical light-curve for the most favourable orientation is shown with black solid lines. Red error bars are 1σ confidence intervals.

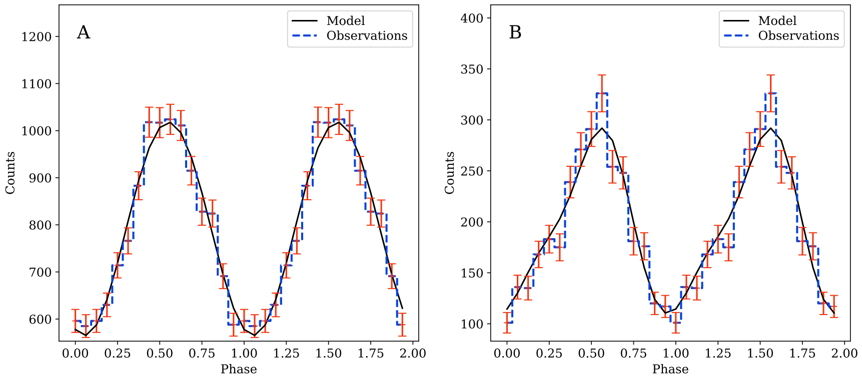

Figure 6: **Folded soft X-ray light-curve (300-2000 eV) for magnetars.** A panel: XTE J1810–197, B panel Swift J1822.3-1606. Dashed blue lines show observations, and the theoretical light-curve for the most favourable orientation is shown with black solid lines. Red error bars are 1σ confidence intervals.

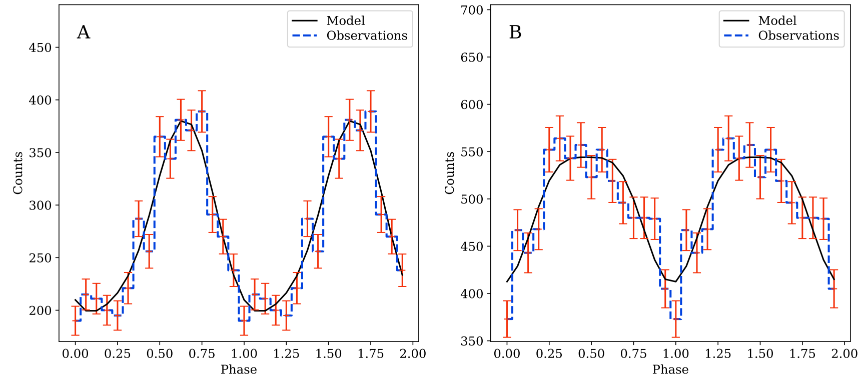

Figure 7: **Folded soft X-ray light-curve (300-2000 eV) for magnetars.** A panel: CXOU J171405.7-381031, B panel SGR 1900+14. Dashed blue lines show observations, and the theoretical light-curve for the most favourable orientation is shown with black solid lines. Red error bars are 1σ confidence intervals.

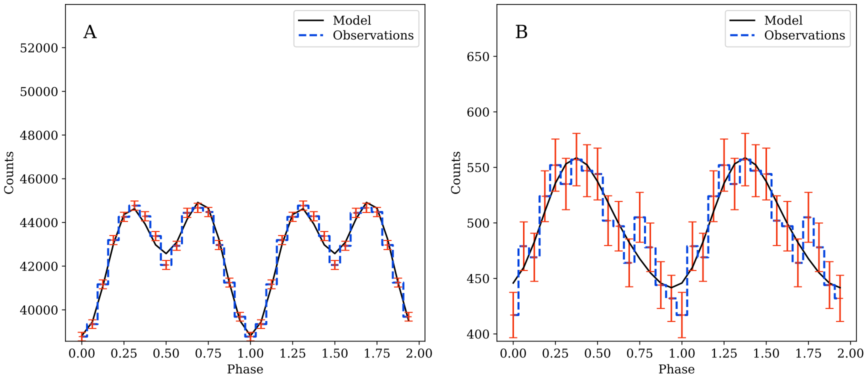

Figure 8: **Folded soft X-ray light-curve (300-2000 eV) for magnetars.** A panel: 4U 0142+61, B panel 1E 1841-045. Dashed blue lines show observations, and the theoretical light-curve for the most favourable orientation is shown with black solid lines. Red error bars are 1σ confidence intervals.

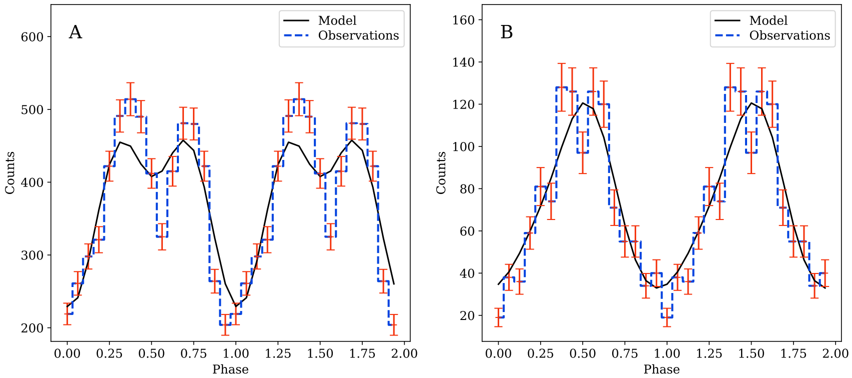

Figure 9: **Folded soft X-ray light-curve (300-2000 eV) for magnetars.** A panel: SGR 0501+4516, B panel 3XMM J185246.6+003317. Dashed blue lines show observations, and the theoretical light-curve for the most favourable orientation is shown with black solid lines. Red error bars are 1σ confidence intervals.

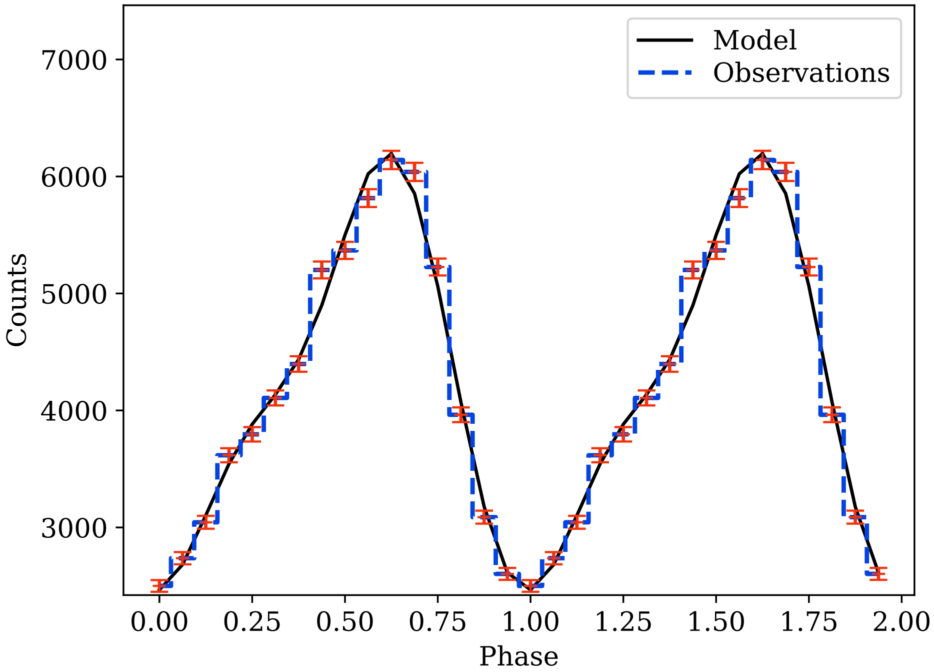

Figure 10: **Folded soft X-ray light-curve (300-2000 eV) for 1RXS J170849.0–400910.** The dashed blue lines and red error bars are observations and 1σ confidence intervals. The solid black lines are the theoretical light-curve for the most favourable orientation.